



# Influence of Deformation Temperature On Flow Stress and Dislocation Structure of 2A12 Aluminum Alloy Under Quasi-Static and Dynamic Compression

Z. Fan<sup>1</sup> · Z. Song<sup>2</sup> · D. Xiao<sup>3</sup> · G. Ribárik<sup>4</sup> · T. Ungár<sup>4,5</sup>

Received: 5 July 2022 / Accepted: 17 February 2023 / Published online: 24 March 2023  
© Society for Experimental Mechanics 2023

## Abstract

**Background** In many constitutive models for dynamic strain aging of aluminum alloys, the athermal component of flow stress was commonly assumed to be independent of temperature and strain rate. However, the assumption has not been examined experimentally due to lacking of a reliable and quantitative method to obtain statistical information of dislocation structure in the deformed aluminum alloys.

**Objective** Develop a novel X-ray diffraction procedure to characterize the evolution of dislocation structure in aluminum alloys over a wide range of temperatures and strain rates, and further clarify the contributions arising from the structural and thermal components of flow stress.

**Methods** The quasi-static and dynamic compression of artificial aged 2A12 aluminum alloy was carried out at the strain rates of  $5 \times 10^{-3}$  and  $1 \times 10^3 \text{ s}^{-1}$  and within a temperature range of 173–673 K. The dislocation structure in the deformed aluminum alloy was determined by the newly developed X-ray line profile analysis procedure (CMWP). In combination with mechanical and X-ray diffraction tests, the correlation between the flow stress and microstructure for the aluminum alloy was established.

**Results** X-ray diffraction measurements showed the dislocation density in the deformed 2A12 aluminum alloy is temperature and strain rate dependence. Besides the structural or athermal component of flow stress calculated from the measured microstructure parameters, a bell-shaped flow stress was revealed clearly in the total flow stress, which can be attributed primarily to the dynamic strain aging mechanism.

**Conclusions** In this work, a fairly concise routine was proposed to characterize the microstructure and estimate the deformation mechanism for the 2A12 aluminum alloy, and the methodology could be easily extended to other alloys.

**Keywords** 2A12 aluminum alloy · Compression · Dislocation structure · Dynamic strain aging · X-ray line profile analysis

## Introduction

2A12 aluminum alloy is one of important Al-Cu-Mg series alloys, which has nearly similar composition as that of 2024 aluminum alloy but with different heat treatment processes [1–3]. It becomes widely used structural material in aerospace, aircraft, marine and automotive industries because of excellent comprehensive properties of specific strength, heat conductivity, corrosion resistance, ductility and fracture toughness [4, 5]. Structural components composed of aluminum alloys usually experience complex circumstance conditions, such as extreme temperatures and strain rates. All these factors will influence mechanical response of materials and eventually stability of components. In order to improve the performance and reliability of structural components, it's fundamental to know the mechanical behavior

✉ Z. Fan  
fanzhijian@caep.cn

<sup>1</sup> Key Laboratory of Neutron Physics and Institute of Nuclear Physics and Chemistry, China Academy of Engineering Physics, Mianyang 621999, China

<sup>2</sup> Institute of Fluid Physics, China Academy of Engineering Physics, Mianyang 621999, China

<sup>3</sup> Institute of Materials, China Academy of Engineering Physics, Mianyang 621999, China

<sup>4</sup> Department of Materials Physics, Eötvös University, Budapest, P.O.Box 32, H-1518, Hungary

<sup>5</sup> School of Materials, The University of Manchester, Manchester M13 9PL, UK

and microstructure evolution of aluminum alloys over a wide range of temperatures and strain rates.

The relationship between flow stress and deformation conditions, including temperature, strain rate and strain, is usually depicted by a constitutive equation. Many constitutive models have been developed and applied to estimate the flow properties of aluminum alloys [6–12]. In the work of Lin et al. [9], a phenomenological constitutive model based on the Johnson-Cook model [13] and Arrhenius type model was proposed to evaluate the flow stress of Al-Cu-Mg alloys subjected to hot forming processes. In contrast to the Johnson-Cook model, the coupled effects of strain hardening, strain rate hardening, and thermal softening were considered. In this model, the coefficients used in the strain and strain rate hardening equations are expressed as functions of temperature and strain instead of independent constants in the Johnson-Cook model, and the peak stress changes with Zener-Hollomon parameter. To account for the plastic deformation behavior of the Al-Mg solid solution alloys, Horváth et al. [7] applied the Kubin-Estrin model [14] to predict not only the stress-strain curves but also the dislocation densities of the Al-Mg alloys during the stress controlled uniaxial compression. The predicted dislocation correlated well with that evaluated using the characteristics of Portevin-Le Chatelier effect. Additionally, the study showed both the mobile and forest dislocation densities increased with Mg concentration because of the interaction between the dislocations and solute atoms. Kreyca and Kozeschnik [12] developed a state parameter-based model to mimic the complex mechanical response of Al-Mg alloys at different strains, temperatures and strain rates. In the model, strain hardening is addressed using an extended Kocks-Mecking approach for the evolution of average dislocation density, the yield stress and its dependence on temperature and strain rate is modeled on the combination of the mechanical threshold stress and thermal activation mechanism, where solid solution hardening and dynamic strain ageing is described with a single parameter of effective solute concentration,  $c_{\text{eff}}$ . The stress-strain curves of the Al-Mg alloys with negative strain rate sensitivity were successfully reproduced using the present model with physically-based parameters. Since complex interaction between various microstructures during the deformation of Al alloys, characterizing accurately the evolution of microstructure is essentially necessary for both the deep insight of deformation mechanism and the validation of the physically-based constitutive models of materials.

As one of effective characterization methods, X-ray line profile analysis can provide the statistical properties of microstructure in crystalline materials [15, 16]. Recent years, the convolutional multiple whole profile (CMWP) procedure [17–19] has been developed for the evaluation of X-ray diffraction data, and the density, character and arrangement parameter of dislocations, the type and

probability of twin/stacking fault, and crystallite size can be obtained. In order to investigate the effect of severe plastic deformation on the microstructure and mechanical properties of Al-Mg alloys, dislocation densities and crystallite size have been determined by X-ray line profile analysis [20]. It was observed that a huge number of dislocations and small subgrain size were developed and reached a stable state with increasing strain. Fátay et al. [21] studied the thermal stability of the deformation induced defects in a deformed Al-Mg-Sc-Zr alloy. When the heat treatment temperature increased, the decreasing rate of dislocation densities was quicker than the increasing rate of crystallite size. As for polycrystalline Al alloys, the texture component, such as cube, goss, copper and brass, can be formed during the manufacturing processes. In the Ref. [22], as a function of annealing temperature the evolution of the dislocation density and the subgrain size for each texture component in a cold-rolled Al-0.2Sc-0.1Zr alloy were determined using line profile analysis in combination with texture information. It showed that the recovery rates of the microstructure in all the texture components of the alloy were similar in the temperature range from the ambient to 573 K.

Although great efforts on measuring microstructure of deformed Al alloys have been made using X-ray line profile analysis [20–22], these works mostly focused on the microstructure changes as a function of strain or annealing temperature during low strain rate deformation. Studies showed that strain rate in plastic deformation can also influence dislocation density and grain size [23–25]. Synergistic effect of strain, temperature and strain rate on the microstructure and mechanical behavior of Al alloys were seldomly investigated. The main problem is the lack of a reliable and feasible method to quantify the contribution arising from different conditions separately. Especially, commercial product of Al alloys usually has heterogeneous microstructures with textures and precipitation particles, which bring nontrivial work for dealing with X-ray diffraction patterns. To improve the computation process of diffraction patterns, the CMWP has been updated newly by extending or developing some novel functions, which includes weighting scheme selection and global optimization by using the combination of Monte-Carlo and Levenberg-Marquardt algorithms [19]. This will shed light on obtaining more reliable microstructure results and further establishing a solid foundation for the constitutive modelling of Al alloys.

In the current research we investigate the flow stress of an extruded 2A12 aluminum alloy compressed using universal material testing machine and Hopkinson bar. The range of deformation temperature covers 173–673 K and strain rates are  $5 \times 10^{-3}$  and  $1 \times 10^3 \text{ s}^{-1}$ , respectively. The relationship between the flow stresses of the Al alloy and the temperatures and strain rates was revealed. The microstructure of the samples was observed by transmission electron microscopy

(TEM) and X-ray diffractometer. The CMWP procedure was used to evaluate the diffraction patterns and obtain the density and arrangement parameter of dislocations and sub-grain size. The deformation mechanism of the specimens was discussed in terms of the correlation between the flow stress and the microstructure.

## Experimental

### Samples

The samples of 2A12 aluminum alloy were obtained from Southwest Aluminium (Group) Co., Ltd.. The chemical composition of the samples in wt% is: Cu: 4.3, Mg: 1.5, Mn: 0.6, Fe: 0.3, Si: 0.2, and the balanced is Al. The heat treatments including solution annealing, quenching and artificial ageing were carried out for the samples. The specimens were aged at 463 K for 10 h for obtaining fine precipitates so as to strengthen the materials. The cylindrical specimens with 10 mm diameter and 10 mm height were quasi-static and dynamic compressed at different temperatures, respectively. Before the compression, the sample was maintained in a thermostat for 12 min at the preestablished temperature. The quasi-static compression was carried out in a universal materials testing machine. The strain rate of  $5 \times 10^{-3} \text{ s}^{-1}$  and the temperatures of 173, 223, 293, 423, 503, 553 and 573 K were applied, respectively. The dynamic compression was performed using a split Hopkinson pressure bar with 22 mm diameter. The experimental setup of the Hopkinson bar is illustrated in Fig. 1. Firstly, the incident and transmission bars were driven by a pneumatic mounting system in opposite directions to contact the sample. To avoid elastic modulus change of the guide bars, the cold contact time for the bars and the specimen was about tens of milliseconds. The projectile collided with the incident bar at a speed of  $\sim 15 \text{ m/s}$ , a rectangular stress pulse was produced and transmitted into the tested sample. The averaged strain and stress of the sample are therefore calculated from the measured stress pulses of the incident and transmission bars by the

strain gauges. For the dynamic compression, the samples were deformed at the strain rate of  $1 \times 10^3 \text{ s}^{-1}$  and the temperatures of 293, 423, 503, 553, 573 and 673 K, respectively. It is assumed during plastic deformation the sample volume remained constant and the deformation along the sample length was uniform. The relations  $\sigma = \sigma_E(1 - \epsilon_E)$  and  $\epsilon = -\ln(1 - \epsilon_E)$  can be applied to obtain true-stress vs. true-strain curves, where  $\sigma$ ,  $\epsilon$  and  $\sigma_E$ ,  $\epsilon_E$  correspond to the values of true-stress, true-strain and engineering-stress, engineering-strain, respectively. Fig. 2 shows the true-stress vs. true-strain curves of the quasi-static and dynamic compressed samples at different temperatures.

### Electron Microscopy and X-ray Diffraction Measurements

After the deformation, the samples deformed at 173, 293, 423, 573 K and  $5 \times 10^{-3} \text{ s}^{-1}$  and at 293, 423, 503, 573, 673 K and  $1 \times 10^3 \text{ s}^{-1}$  were selected, and the surface of the central part of the samples perpendicular to the compression direction were prepared for the X-ray diffraction measurements. X-ray diffraction patterns were measured using an X-ray diffractometer (PANalytical X'Pert PRO) working at 40 kV and 40 mA. The focal spot size and the take-off angle are  $0.4 \text{ mm} \times 12 \text{ mm}$  and  $6^\circ$ , respectively. The distance of incident and diffracted beam path is 240 mm for Bragg-Brentano geometry. The angle of the divergence slit is set to  $0.5^\circ$  and the size of the receiving slit is 0.05 mm. A nickel filter was used to remove  $K_\beta$  radiation, and then  $K\alpha_{1,2}$  doublet was received by an X'Celerator detector. The  $2\theta$  angular range of the measured diffraction patterns is  $30^\circ$ - $120^\circ$  and the step length is  $0.033^\circ$ . The  $K\alpha_2$  lines were stripped using the Rachinger algorithm before the line profile analysis. A NIST SRM 640d silicon powder was measured for the evaluation of the line profiles of the instrument. To observe the morphology of dislocations and precipitates in the samples, the TEM analysis was carried out in a FEI Tecnai FEG-TEM operating at 200 kV. All the thin-foil specimens were prepared by the mechanical polishing and twin-jet electro polishing. The

**Fig. 1** Schematic of the experimental setup for dynamic compression

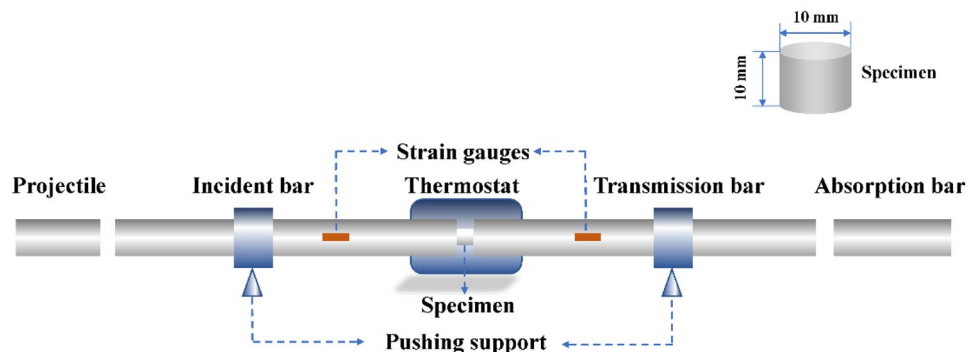
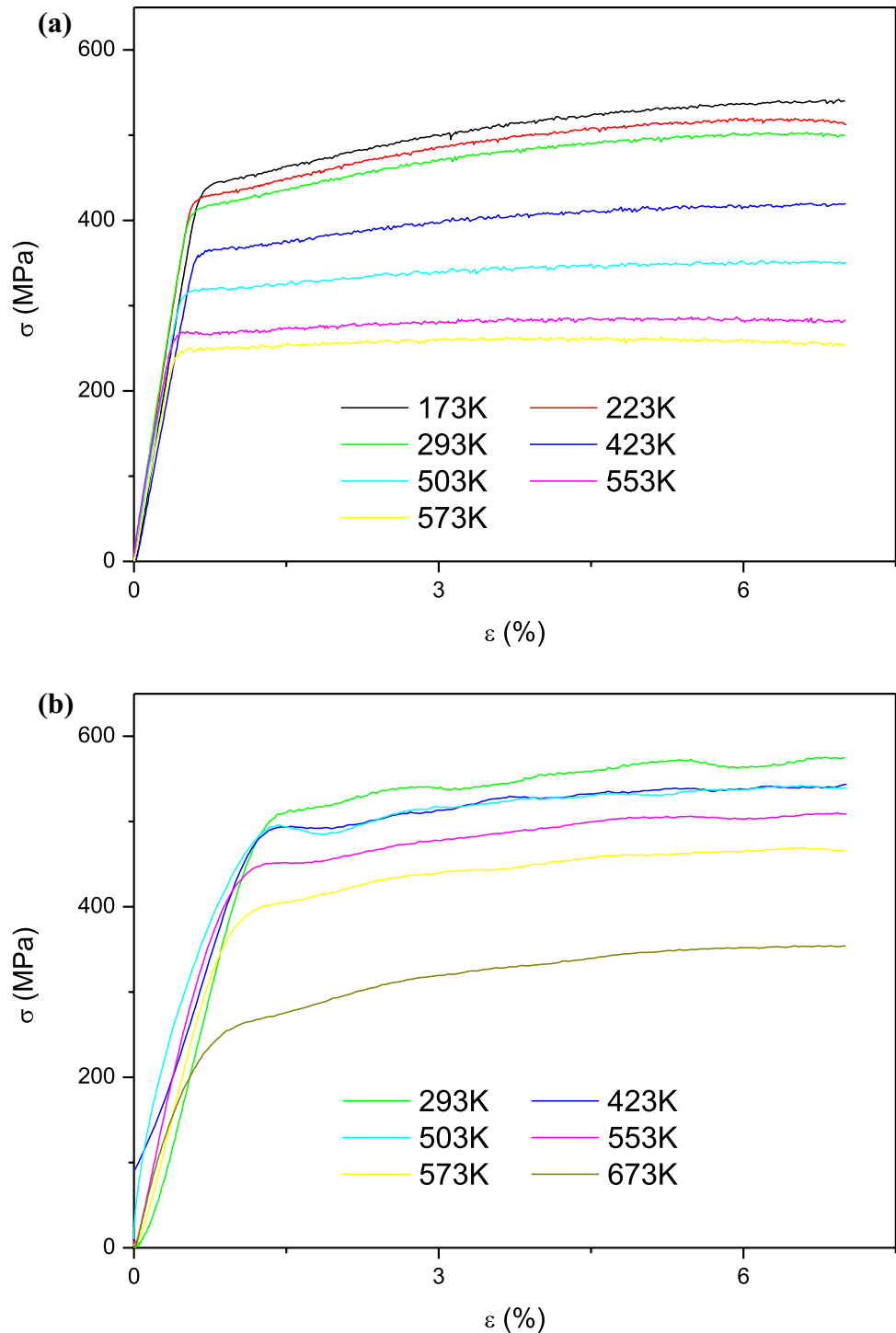


**Fig. 2** True-stress vs. true-strain curves of the quasi-static (a) and dynamic (b) compressed 2A12 aluminum alloy samples at different temperatures

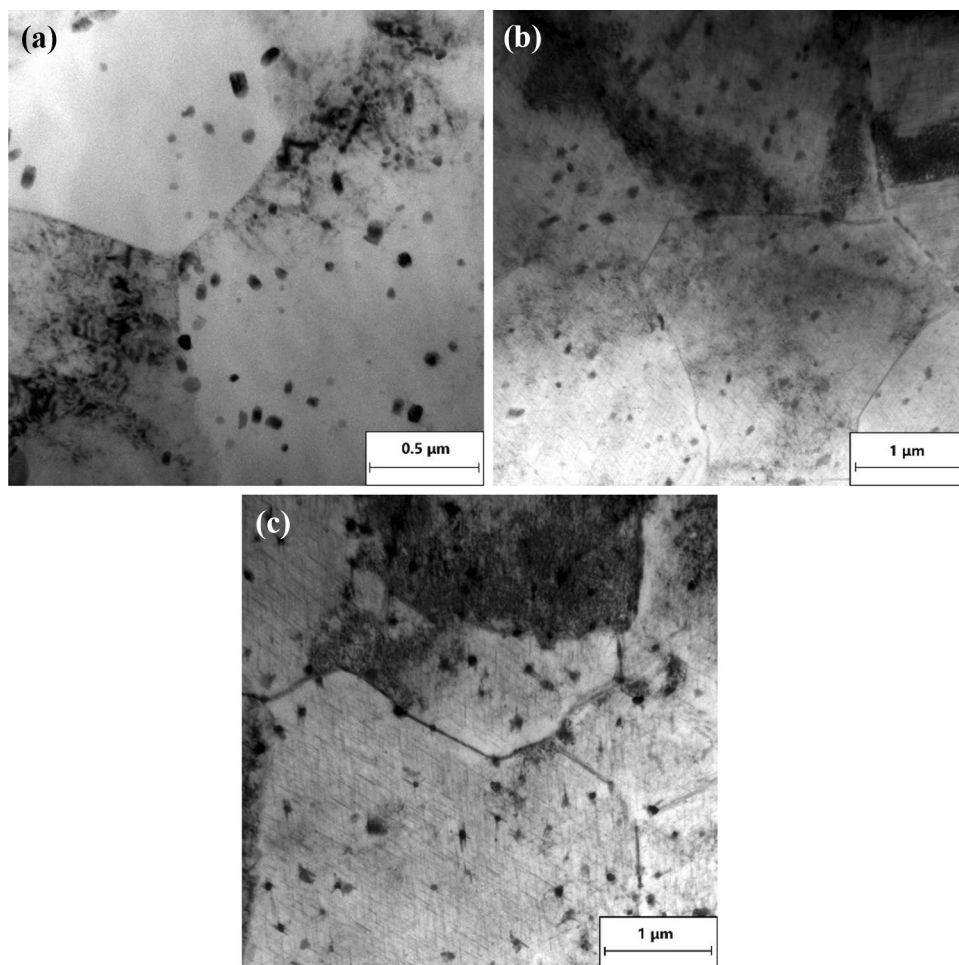


TEM micrographs of the initial specimen and the specimen deformed at 573 K and  $5 \times 10^{-3} \text{ s}^{-1}$  and deformed at 673 K and  $1 \times 10^3 \text{ s}^{-1}$  are shown in Fig. 3, where the size of the grains and the precipitates are about 2  $\mu\text{m}$  and 60 nm and the dislocations are distributed inside the crystallites.

### Evaluation of the X-ray Diffraction Patterns

The X-ray diffraction patterns are broadened due to crystallite size, lattice distortions as well as instrumental effects. The effect of lattice distortions and crystallite size on peak

**Fig. 3** TEM micrographs of the initial specimen (a) and the specimen deformed at  $5 \times 10^{-3} \text{ s}^{-1}$  and 573 K (b) and deformed at  $1 \times 10^3 \text{ s}^{-1}$  and 673 K (c). The scale length in (a) is 0.5  $\mu\text{m}$  and in (b) and (c) is 1  $\mu\text{m}$ , respectively



broadening can be compared qualitatively using the method of the Williamson-Hall (WH) plots [26]. The WH plots of the quasi-static and Hopkinson bar compressed Al alloy

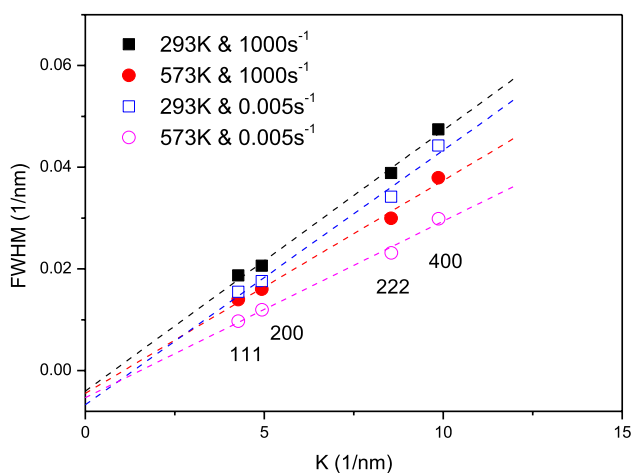


**Fig. 4** The Williamson-Hall plots of the quasi-static and Hopkinson bar compressed Al alloy samples at the deformation temperature of 293 and 573 K, where the dash lines are the linear fitted lines for the corresponding samples

samples at the deformation temperature of 293 and 573 K are shown in Fig. 4, respectively. In the figure, the full widths at half maximum (FWHM) of physical profiles are plotted vs.  $K = 2\sin\theta/\lambda$ , where the FWHM values are obtained after subtracting the instrument broadening from the measured diffraction peaks of the Al alloy samples,  $\theta$  and  $\lambda$  are the diffraction angles and the X-ray wavelength, respectively. The dash lines in the WH plots are the linear fitted lines where the slope is proportional to the microstrain and the intercept on the ordinate is inversely proportional to the crystallite size. It can be seen that the microstrain increases with increasing the strain rate or decreasing the deformation temperature. In the same time, we found crystallite sizes from the intercepts are negative values which are certainly lacking of physical significance. This is because the theoretical assumptions implicated in the WH plots are incomplete. In order to obtain accurately the microstructure information not only the FWHMs but also the line profiles should be taken into account. This is the work that the CMWP line profile analysis procedure try to deal with.

In the evaluation of CMWP, the measured diffraction patterns are matched by the convolution of the physical profiles



and the instrumental profiles. The instrumental profiles were taken from the measurement of the NIST SRM 640d silicon powder sample. The physical profiles are related with crystallite size and lattice defects [15, 18]. The size profile is obtained by assuming that crystallite sizes follow a lognormal distribution, which can be written as [27]:

$$I(s) = \int_0^{\infty} x \frac{\sin^2(x\pi s)}{(\pi s)^2} \operatorname{erfc} \left[ \frac{\log(x/m)}{\sqrt{2}\sigma_{LN}} \right] dx \quad (1)$$

where  $s = 2(\sin\theta - \sin\theta_B)/\lambda$ ,  $\theta_B$  is the exact Bragg angle,  $m$  and  $\sigma_{LN}$  are the median and the variance of the lognormal distribution. The area average mean crystallite size or coherent domain size  $d_x$  is determined as [28]:

$$d_x = m \exp \left[ (5/4) \left( \sqrt{2}\sigma_{LN} \right)^2 \right] \quad (2)$$

The defect profile is diffraction profile comes from various kind of lattice defects including dislocations, twins and stacking faults. Since few planar defects were observed in the coarse-grained Al alloy samples, we considered exclusively the diffraction effect of dislocations in the present case. The Fourier coefficient of defect profile can be written as [29, 30]:

$$A^D = \exp \left( -2\pi^2 L^2 g^2 \langle \varepsilon_{g,L}^2 \rangle \right) \quad (3)$$

where  $g$  and  $L$  are the length of the diffraction vector and the Fourier variable,  $\langle \varepsilon_{g,L}^2 \rangle$  is the mean square strain arising from dislocations. The expression of  $\langle \varepsilon_{g,L}^2 \rangle$  [30] is

$$\langle \varepsilon_{g,L}^2 \rangle = \frac{\rho \bar{C} b^2}{4\pi} f(L/R_e) \quad (4)$$

where  $\rho$ ,  $b$ ,  $\bar{C}$  and  $R_e$  are the density, the Burgers vector, the average contrast factor and the effective outer cut-off radius of dislocations,  $f(L/R_e)$  is the Wilkens function. In the case of a texture-free polycrystalline or all possible Burgers vectors are activated, the dislocation contrast factors can be averaged over the permutations of the multiplicity of the  $hkl$  reflections and the average contrast factors  $\bar{C}_{hkl}$  for cubic crystals are given as [31]:

$$\bar{C}_{hkl} = \bar{C}_{h00} (1 - qH^2) \quad (5)$$

where  $\bar{C}_{h00}$  is the average contrast factor for the  $h00$  reflections,  $q$  is a parameter depending on the character of dislocations and the elastic constants of the sample [17, 32] and  $H^2 = (h^2k^2 + h^2l^2 + k^2l^2)/(h^2 + k^2 + l^2)$ . The defect profile due to dislocations can be directly given by the Fourier transform of  $A^D$ .

As shown in equations (1)–(5), the best solutions of five parameters for the samples need to be searched in the optimization process of CMWP. These parameters are the median,

$m$ , and the logarithmic variance,  $\sigma_{LN}$  of the lognormal size distribution and the density,  $\rho$ , the effective outer cut-off radius,  $R_e$ , and the parameter,  $q$  of dislocations. During the iterations, the theoretical diffraction pattern was calculated using the parameters and compared with the measured diffraction pattern. Once the relative change of the residuals of the measured and calculated patterns between two iteration steps is less than the predefined criteria or the maximal number of iterations is reached, the evaluation procedure will stop. To obtain the character of dislocations in cubic crystals, the theoretical  $q$  values for the edge and screw dislocation were numerically calculated by a program ANIZC [32]. Comparing the measured and the theoretical values of the  $q$  parameter, one can obtain slip activity of dislocations in the samples. Finally, the CMWP procedure can provide the densities, characters and arrangement of dislocations and the subgrain size in the deformed Al alloy samples.

Figure 5 shows typical CMWP evaluated diffraction patterns of the Al alloy samples deformed at room temperature and 573K using a Hopkinson bar, where the intensity is plotted in logarithm scale. As shown in Fig. 5, the diffraction pattern of the Al alloy specimen is composed of the {111} and {200} reflection families with stronger intensities, and the other reflections with weaker intensities. It can be concluded that the current studied Al alloy samples possess {111} and {200} fiber texture components, which is ubiquitous for the extruded Al alloy bar. In principle, the reflections corresponding to different texture components should be considered independently in the calculation. However, we still take the average contrast factor as a suitable approximation because of the following considerations: (i) The elastic constants of Al are  $c_{11} = 108.2$  GPa,  $c_{12} = 61.3$  GPa and  $c_{44} = 28.5$  GPa [33], respectively. The Zener constant,

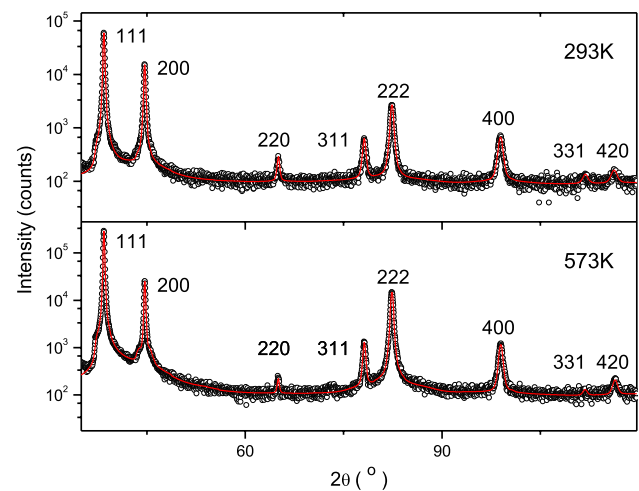


**Fig. 5** The measured (open circles) and the CMWP evaluated (solid line) diffraction patterns of the Al alloy samples deformed at 293K and 573K using a Hopkinson bar. The intensity is shown in logarithm scale

$A_z = 2c_{44}/(c_{11} - c_{22})$ , of Al is about 1.2, indicating that the elastic anisotropy is comparably small; (ii) when multiple slip systems are activated at larger deformation and/or higher temperature the individual contrast factor values of the *hkl* reflections become closer to the average contrast factor [34]; (iii) it's shown the dislocation densities are nearly the same for all the grain orientations in a tensile deformed stainless steel at the larger deformation after stage-II work hardening [35], which justify the dislocation densities in the texture components could be *hkl* orientation independent.

## Results

### Plastic Flow Behavior of 2A12 Al Alloy

The true-stress versus true-strain curves of the Al alloy samples after a deformation of ~7% strain are shown in Fig. 2. In the elastic deformation region, the deviation between the stress-strain curves is comparably larger for the dynamic compression than for the quasi-static compression. Especially, the stress-strain curve for the dynamic compression at 423K even did not begin with zero stress. It is mainly because the mismatches of the diameter and sound impedance between the guide bars and the sample, the stress-strain curve for the dynamical compression can't be obtained accurately at the stage of elastic deformation. After yielding, the flow stress increases with plastic strain due to work and strain rate hardening. To observe quantitatively the effect of strain rate and temperature on the plastic deformation of 2A12 Al alloy, a comparison was made in Fig. 6 for the change of flow stress as a function of temperature at the strain rates of  $5 \times 10^{-3}$  and  $1 \times 10^3$  s<sup>-1</sup>.

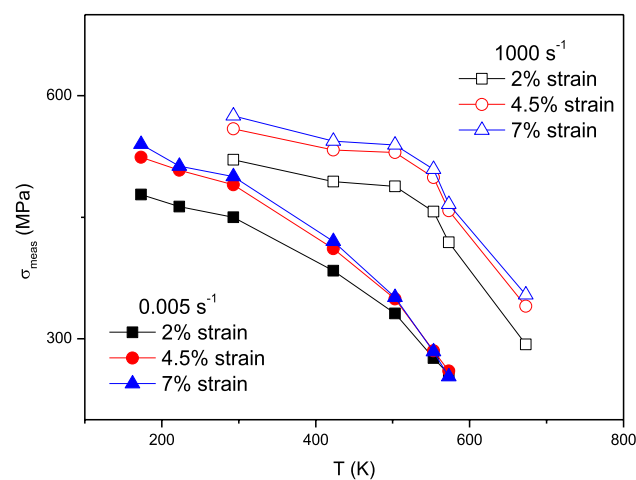


**Fig. 6** Flow stress vs. deformation temperature at the strain rates of  $5 \times 10^{-3}$  and  $1 \times 10^3$  s<sup>-1</sup>. The flow stresses were taken at the strains of 2%, 4.5% and 7%, respectively

The flow stresses were taken at the strains of 2%, 4.5% and 7%, respectively. At both the strain rates, the samples all appeared to be softened with the temperature increasing. For the quasi-static compression at 7% strain, the flow stress decreased along the variation of temperature, which is 540 MPa at 173 K and then continuously dropped to 253 MPa at 573 K. For the Hopkinson bar compression at 7% strain, the flow stress is higher than that of the quasi-static compression due to about five order increase of strain rate. However, the flow stress seems insensitive to the temperature below 503 K, which evolved from 575 MPa at 293 K to 354 MPa at 673 K. The thermal-activated mechanism [36] plays an important role in determining the flow behavior of the samples. When the temperature rises, thermal energy lowers down the effective height of short-range barriers and accordingly the flow stress decreases. The increase of strain rate has a negative effect of temperature on the material softening because of less time for thermal energy to get across short-range barriers, therefore higher flow stress has to be applied. At a higher temperature, e.g., 573 K for the quasi-static compression, the flow stress is closer to the athermal component. This indicates at the moment short-range barriers have been overcome almost by thermal energy, and the flow stress is determined mainly by the long-range barriers.

### Microstructure of the Compressed Specimens

The diffraction patterns of the selected Al alloy samples were evaluated using the CMWP procedure. The dislocation density  $\rho$  and the subgrain size  $d_x$  as a function of deformation temperature are shown in Fig. 7. For the quasi-static compression, the dislocation density is  $1.0 \times 10^{15}$  m<sup>-2</sup> at the temperature of

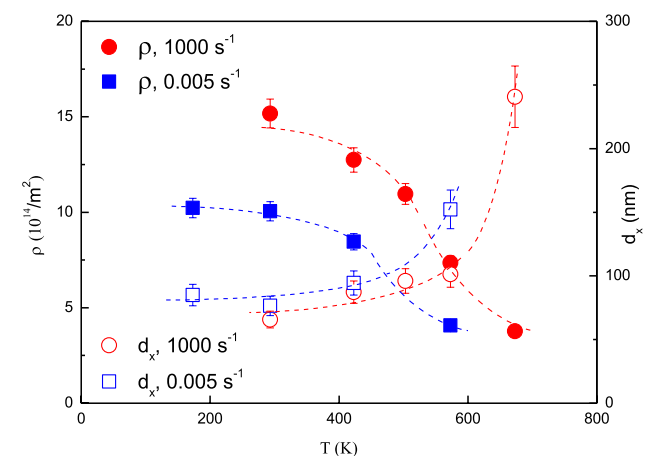


**Fig. 7** Dislocation density  $\rho$  and area average mean crystallite size  $d_x$  of the Al alloy specimens deformed at the strain rates of  $5 \times 10^{-3}$  and  $1 \times 10^3$  s<sup>-1</sup> vs. the deformation temperature. The dashed lines are to guide the eye

173 K, then a slight decrease proceeds up to 423 K, after that a drop-off occurs and it reaches a low value of  $0.4 \times 10^{15} \text{ m}^{-2}$  at 573 K. For the Hopkinson bar compression, the dislocation densities follow a similar decreasing trend of first slowness and then rapidness, which starts from  $1.5 \times 10^{15} \text{ m}^{-2}$  at the 293 K to  $0.4 \times 10^{15} \text{ m}^{-2}$  at 673 K. In contrast to the dislocation densities, after a gentle increase from a level about 80 nm with the temperature increasing, the subgrain size rises dramatically to 150 and 240 nm for the quasi-static and Hopkinson bar compression, respectively. The dislocation arrangement parameter  $M = R_e \sqrt{\rho}$  describes the mutual screening ability of the dislocation strain fields. When the dislocations have stronger dipole character or weaker long-range strain fields, the  $M$  values become smaller. The evolution of the  $M$  parameters as a function of temperature is shown in Fig. 8. The character of dislocations in the samples can be determined by the  $q$  parameter, which accounts for the anisotropic peak broadening due to dislocations. For the Al alloy samples, the theoretical  $q$  values are 0.37 and 1.35 corresponding to the edge and screw character of  $a/2\langle 111 \rangle\{110\}$  slip system, respectively. As illustrated in Fig. 9, the experimental  $q$  values provided by CMWP fluctuate in the range of 0.4 and 0.7, indicating that the dominate character of dislocations in the samples is edge.

## Discussion

### Effects of Temperature and Strain Rate On the Evolution of Dislocation Density

When the Al alloy samples are compressed, both the multiplication and annihilation of dislocations occur simultaneously during the compression. Comparing the measured

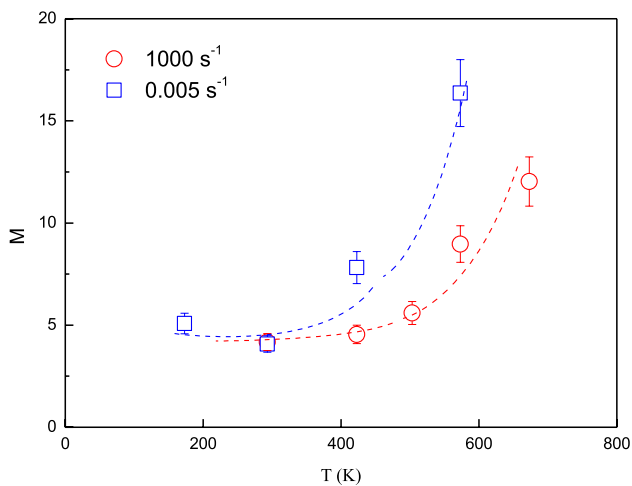


**Fig. 8** Dislocation arrangement parameter  $M$  of the Al alloy specimens deformed at the strain rates of  $5 \times 10^{-3}$  and  $1 \times 10^3 \text{ s}^{-1}$  vs. the deformation temperature. The dashed lines are to guide the eye

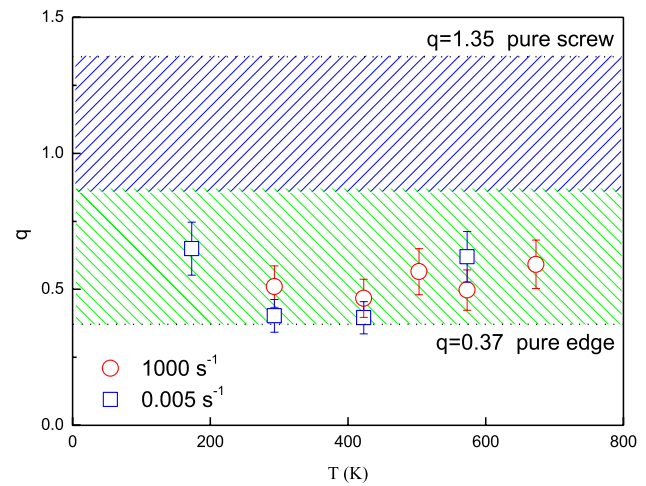


**Fig. 9** Experimental  $q$  parameters of the Al alloy specimens deformed at the strain rates of  $5 \times 10^{-3}$  and  $1 \times 10^3 \text{ s}^{-1}$  vs. the deformation temperature

dislocation densities in the samples after the deformation at different temperatures, if the temperature is less than  $\sim 423$  K for the quasi-static compression and  $\sim 503$  K for the Hopkinson bar compression, the dislocation densities in the samples decrease moderately. It indicates the dislocation structure generated in the deformation process is still fairly stable within these temperature ranges. As the deformation temperature increases further, the dislocation densities drop dramatically up to the temperature of 573 and 673 K for the quasi-static and the Hopkinson bar compression, respectively. The descending of dislocation densities could be attributed primarily to the effect of thermal activation [36]. In the plastic deformation of an alloy, mobile dislocations will meet various kinds of possible resistances, e.g., Peierls-Nabarro force, crossing of forest dislocations, elastic interaction between dislocations, precipitates and etc., which can be classified into short- and long-range barriers depending on interaction distance of strain field. It's well known that temperature has a large impact on short-range barriers. The height of short-range barriers will be reduced if temperature increases. For the 2A12 Al alloy samples with face-centered cubic structure, short-range barriers mostly consist of forest dislocations, and the width of extended dislocation is narrow and inclined to be bounded due to high stacking fault energy of aluminum. The increasing temperature accelerated the diffusion of point defects, cross-slip and climb of dislocations, and correspondingly enhanced dynamic recovery of dislocations. This resulted in the rapid annihilation of dislocations at the higher temperatures.

Besides temperature, the quantity of dislocations in the Al alloy samples is also strongly dependent on strain rate. As shown in Fig. 7, although the evolution trend of dislocations is similar for both the quasi-static and Hopkinson bar



compression, there is remarkably different between them. Before the deformation temperature of 573 K, the dislocation densities in the samples after the quasi-static compression are almost ~30% less than those after the Hopkinson bar compression at the same temperature. As the strain rate rises, the applied external force has to be increased to facilitate dislocation movement, a large number of dislocations are activated and multiplied, however the time for dislocation annihilation is insufficient. Therefore, the incomplete dynamic recovery resulted in high dislocation densities left in the samples deformed at the higher strain rate. Additionally, in Fig. 7 we can find the dislocation density at the deformation temperature of 573 K for the quasi-static compressed sample is very close to that at the deformation temperature of 673 K for the Hopkinson bar compressed sample. The temperature difference about 100 K can also be explained by the shorter time for dislocations to overcome short-range barriers at the higher strain rate. To compensate the weakening effect of thermal energy, higher temperatures are needed to promote the annihilation of dislocations.

### The Relation Between the Subgrain Size and the Dislocation Arrangement

As shown in Fig. 7, the subgrain size was changed in an opposite direction of the dislocation densities for both the quasi-static and Hopkinson bar compression. It's noted that the subgrain size determined by X-ray diffraction are not certainly equal to the crystallite size obtained from TEM [37]. The crystallite size from TEM is ~2  $\mu\text{m}$ , which is one order larger than the subgrain size from X-ray diffraction. As illustrated in the Ref. [27, 37], there is a sequence of length scales in a bulk material, the TEM size usually corresponds to the grains with large angle boundaries while the X-ray size to the coherently scattering domains divided by 1-2 degrees of small angle misorientation. For the 2A12 Al alloy samples, there're dispersed hard precipitates distributed in the soft Al matrix. The dislocations pinned by the precipitates could produce local misorientations randomly. According to the TEM measurements, the interval between the precipitates is about 200 nm, which is in good correlation with the subgrain size determined from X-ray diffraction. Besides the precipitates, the solute atoms also have strong pinning effect of dislocations, which was substantiated by the character of dislocations in the samples. As discussed in paragraph 3.2, the dislocations are mostly of edge character. This result together with other previous investigations [20, 38] shows if there're solute atoms prevailing in the materials, edge dislocations could be pinned preferentially and the dislocation character will be shifted to the edge type after a deformation.

Since the subgrain size obtained from X-ray diffraction is coherently scattering domains divided by dislocation arrays,

the evolution of subgrain size with temperature is essentially related to both the density and arrangement of dislocations. At the low temperatures, the change of dislocation densities is moderate in the deformation, which means most dislocations are pinned or tangled and difficult to move. Correspondingly, the subgrain size is stable with temperature as well. If the temperature is elevated higher than a critical value, e.g., ~503 K at  $5 \times 10^{-3} \text{ s}^{-1}$  and ~573 K at  $1 \times 10^3 \text{ s}^{-1}$ , the dynamic recovery become more remarkable and dislocations tend to break away obstacles and glide. The annihilation of dislocations and the growth of subgrains lead to a reduction of the stored energy in the samples. Here, we focus on the relation between the dislocation arrangement parameter  $M$  and the subgrain growth with temperature. When the samples were compressed at the lower temperatures, a large number of dislocations accumulated and arranged into low energy configurations. At this stage, the  $M$  parameters are comparable small, indicating stronger dipole character of dislocations. When the temperature increases, the dislocation dipoles come closer and annihilate finally [38], resulting the  $M$  parameters increase significantly. Meanwhile, the excess dislocations with the same signs can't be annihilated, which will be driven to migrate and form low angle grain boundaries. Therefore, the subgrain growth at the higher temperatures occurs concomitantly with the increase of the  $M$  parameters. The subgrain sizes are 150 nm for the quasi-static compression at 573 K and 240 nm for the Hopkinson bar compression at 673 K, respectively, which is close to the intervals between the precipitates. The precipitates distributed in the samples could hinder the further coalescence of the subgrains.

### Correlation Between the Flow Stress and Microstructure

As discussed in the paragraph 4.1, the flow stress of the present 2A12 Al alloy samples deformed at different strain rates and temperatures consists of structural component and thermal component. The structural component  $\sigma_s$  is directly related with the microstructure in the samples, including grain size, dislocations and precipitates. The thermal component  $\sigma_t$  is a function of strain rate and temperature. Therefore, we correlate the flow stress with the microstructure by adding up different strengthening contributions using the equation:

$$\sigma_{calc} = \sigma_0 + \frac{K}{\sqrt{d}} + \alpha G b M_T \sqrt{\rho} + 0.85 G b M_T \frac{\ln(x/b)}{2\pi(l-x)} + \sigma_t, \quad (6)$$

where  $\sigma_0$  is the friction stress,  $K$  and  $\alpha$  are constants,  $d$  is the grain size determined by TEM,  $G$  is the shear modulus,  $M_T$  is the Taylor factor for polycrystalline material,  $x$  and  $l$  are the average dimension and interval of the precipitates,

respectively. In the right side of equation (6),  $\frac{K}{\sqrt{d}}$  is Hall-Petch type of grain-size contribution [39],  $\alpha G b M_T \sqrt{\rho}$  delineates work-hardening of Taylor mechanism [40],  $0.85 G b M_T \frac{\ln(x/b)}{2\pi(l-x)}$  characterizes precipitation strengthening [41] and  $\sigma_t$  is a term correlated with strain rate and temperature [42].

Since the samples have been artificially aged for 10 h at 190 °C before the deformation tests,  $\sigma_0$  and  $K$  were taken approximately as 20 MPa and 0.040 MPa·m<sup>1/2</sup> for pure Al [41, 43].  $\alpha$  and  $M_T$  were taken as 0.33 and 3 for the polycrystalline specimens,  $b = 0.286$  nm,  $x$  and  $l$  are estimated as 60 and 200 nm from the TEM measurements, the values of  $G$  at the different temperatures are shown in the Table 1. Making use of these parameters, the structural component of flow stress  $\sigma_s$  were calculated and listed in Table 1. The values of thermal component  $\sigma_t$  were obtained by subtracting  $\sigma_0$  and  $\sigma_s$  from the measured flow stresses  $\sigma_{meas}$ . It can be seen in Fig. 10 that the dependence of  $\sigma_t$  on temperature is not a monotonous function, which is more like a bell shape. In the frame of the thermally-activated mechanism the flow stress that getting across the short-range barriers becomes smaller with increasing the temperature, the bell-shaped  $\sigma_t$  can't be explained exclusively by this mechanism. The other mechanism of dynamic strain aging should be taken into account [12, 42, 44–49]. As the deformation of the samples is processing, mobile dislocations could be dragged by the atom atmosphere, such as Cottrell atmosphere [44, 46]. The drag force is determined by the relative velocity between the dislocation moving and the solute atom diffusion. The drag force reached a maximum value when the diffusion velocity of solute atoms is nearly close to the velocity of moving dislocations. When the diffusion is slower or faster than the critical velocity of moving dislocations, the drag force will be decreased. The varying drag force was added as one part of the total flow stress, then we can see the change of  $\sigma_t$  is not a monotonous function of temperature. We fitted the data

**Table 1** The deformation temperature  $T$ , the shear modulus  $G$ , the measured flow stress  $\sigma_{meas}$ , the calculated structural component of flow stress  $\sigma_s$  and the calculated thermal component of flow stress  $\sigma_t$  for the Al alloy specimens deformed at the strain rates of  $5 \times 10^{-3}$  and  $1 \times 10^3$  s<sup>-1</sup>, respectively

Strain rate [s <sup>-1</sup> ]	T [K]	G [GPa]	$\sigma_{meas}$ [MPa]	$\sigma_s$ [MPa]	$\sigma_t$ [MPa]
$5 \times 10^{-3}$	173	28	540	406	114
	293	26	500	377	103
	423	22	420	307	93
	573	17	253	201	32
$1 \times 10^3$	293	27	575	446	109
	423	25	544	392	132
	503	24	539	360	160
	573	22	466	295	151
	673	19	354	217	117

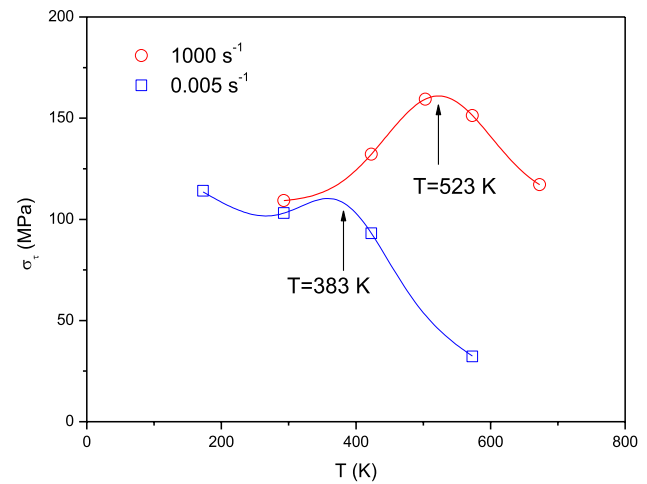


**Fig. 10** Flow stress  $\sigma_t$  vs. deformation temperature of the Al alloy specimens deformed at the strain rates of  $5 \times 10^{-3}$  and  $1 \times 10^3$  s<sup>-1</sup>. The data of  $\sigma_t$  were fitted with a Gaussian function (solid lines), and the temperatures at the peak stress are 383 and 523 K for the strain rates of  $5 \times 10^{-3}$  and  $1 \times 10^3$  s<sup>-1</sup>, respectively

points of  $\sigma_t$  with a Gaussian function, and the calculated values of  $\sigma_t$  were also listed in Table 1. The best match between the measured and calculated flow stress values,  $\sigma_{meas}$  and  $\sigma_{calc}$  are shown in Fig. 11. The temperatures at the peak stress are 383 and 523 K for the strain rates of  $5 \times 10^{-3}$  and  $1 \times 10^3$  s<sup>-1</sup>, respectively. When the strain rate increased from  $5 \times 10^{-3}$  to  $1 \times 10^3$  s<sup>-1</sup>, the temperature of the peak  $\sigma_t$  moved to a higher value. This phenomenon is consistent with the observations in other materials [42, 45, 47]. As the strain rate increased, the mobile dislocations had to move faster. The diffusion of solute atoms needed to be accelerated by higher temperature to catch up with the moving dislocations. Therefore, the temperature region of the dynamic strain aging shifted to a higher temperature region. Within specific temperature regions in Fig. 6 the amplitude

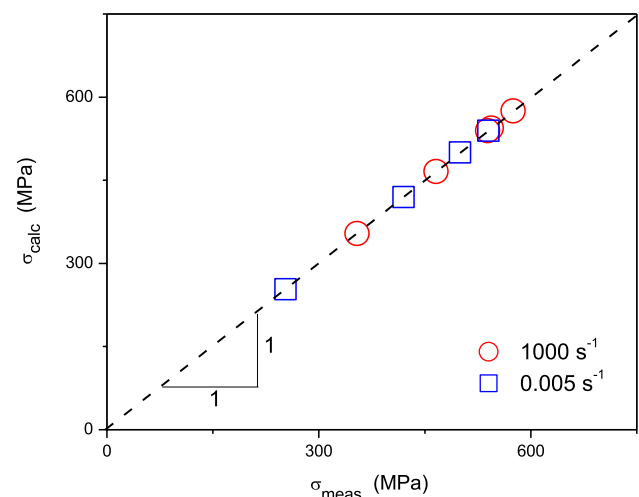


**Fig. 11** The calculated,  $\sigma_{calc}$  vs. the measured,  $\sigma_{meas}$ , flow stress values

of stress peak is not so significant compared to the total flow stress. Kreyca and Kozeschnik [12] compared the flow stress of Al-Mg alloy with 0–5 wt.% solute contents, the peak stress is revealed to be reduced with the descending of solute content. For a full-aged nickel-base superalloy Inconel 718, Yuan et al. [49] attributed a weaker effect of dynamic strain aging to the transformation from the mechanism of shearing to bowing-out between dislocations and precipitates. It is concluded naturally that the artificial aging for the current 2A12 Al alloy samples indeed weaken the peak stress of dynamic strain aging.

## Conclusions

In this investigation the artificial aged 2A12 Al alloy has been uniaxially compressed in a temperature range of 173–673 K and at the strain rates of  $5 \times 10^{-3}$  and  $1 \times 10^3$  s<sup>-1</sup>, respectively. Although the softening of flow stress occurred for the Al alloy samples deformed at both the strain rates, the evolution of flow stress as a function of temperature manifested differently. In contrast to the continuous drop of flow stress in the temperature range of 173–573 K at the strain rate of  $5 \times 10^{-3}$  s<sup>-1</sup>, there's a moderate variation before the temperature of 503 K at the strain rate of  $1 \times 10^3$  s<sup>-1</sup>. In order to correlate the flow stress with the microstructure in the deformed Al alloy samples, TEM and X-ray line profile analysis were used to obtain the size of grains and precipitates and the dislocation density. The structural component of flow stress has been evaluated using the experimentally determined values of the microstructure. After subtracting the structural component from the total flow stress, the left was found to be a bell-shaped flow stress in some specific temperature regions, which shifted to a higher temperature region as the strain rate increased from  $5 \times 10^{-3}$  to  $1 \times 10^3$  s<sup>-1</sup>. The phenomenon was explained well in terms of the dynamic strain aging mechanism.

**Acknowledgements** Z.F. is grateful to the Director Foundation of China Academy of Engineering Physics (Grant No. YZ2019004) and the National Key Research and Development Program of China (No. 2021YFA1600604), Z.S. acknowledges the National Natural Science Foundation of China (Grant No. 11932018), G.R. & T.U. are grateful for the support of OTKA grant K124926 funded by the Hungarian National Research, Development and Innovation Office (NKFIH).

**Data Availability** The data that support the findings of this study are available from the corresponding author upon reasonable request.

## Declarations

**Conflict of Interest** The authors declare no conflict of interest.

## References

- Chen GQ, Liu JP, Shu X, Gu H, Zhang BG, Feng JC (2019) Beam scanning effect on properties optimization of thick-plate 2A12 aluminum alloy electron-beam welding joints. *Mater Sci Eng A* 744:583–592
- Jiang JF, Zhang Y, Wang Y, Xiao GF, Liu YZ, Zeng L (2020) Microstructure and mechanical properties of thixoforged complex box-type component of 2A12 aluminum alloy. *Mater Des* 193:108859
- Zhang HJ, Zhao XH, Liu Y (2021) Effect of high frequency impacting and rolling on fatigue crack growth of 2A12 aluminum alloy welded joint. *Int. J Fatigue* 147:106172
- Nakai M, Eto T (2000) New aspect of development of high strength aluminum alloys for aerospace applications. *Mater Sci Eng A* 285:62–68
- Dursun T, Soutis C (2014) Recent developments in advanced aircraft aluminium alloys. *Mater Design* 56:862–871
- Barlat F, Glazov MV, Brem JC, Lege DJ (2002) A simple model for dislocation behavior, strain and strain rate hardening evolution in deforming aluminum alloys. *Int J Plast* 18:919–939
- Horváth G, Chinh NQ, Gubicza J, Lendvai J (2007) Plastic instabilities and dislocation densities during plastic deformation in Al-Mg alloys. *Mater Sci Eng A* 445–446:186–192
- Fribourg G, Bréchet Y, Deschamps A, Simar A (2011) Microstructure-based modelling of isotropic and kinematic strain hardening in a precipitation-hardened aluminium alloy. *Acta Mater* 59:3621–3635
- Lin YC, Li QF, Xia YC, Li LT (2012) A phenomenological constitutive model for high temperature flow stress prediction of Al-Cu-Mg alloy. *Mater Sci Eng A* 534:654–662
- Khan AS, Liu HW (2012) Variable strain rate sensitivity in an aluminum alloy: Response and constitutive modeling. *Int J Plast* 36:1–14
- Kabirian F, Khan AS, Pandey A (2014) Negative to positive strain rate sensitivity in 5xxx series aluminum alloys: Experiment and constitutive modeling. *Int J Plast* 55:232–246
- Kreyca J, Kozeschnik E (2018) State parameter-based constitutive modelling of stress strain curves in Al-Mg solid solutions. *Int J Plast* 103:67–80
- Johnson GR, Cook WH (1985) Fracture characteristics of three metals subjected to various strains, temperatures and pressures. *Eng Fract Mech* 21:31–48
- Kubin LP, Estrin Y (1990) Evolution of dislocation densities and the critical conditions for the Portevin-Le Chatelier effect. *Acta Metall Mater* 38:697–708
- Warren BE (1959) X-ray studies of deformed metals. *Prog Met Phys* 8:147–202
- Groma I (1998) X-ray line broadening due to an inhomogeneous dislocation distribution. *Phys Rev B* 57:7535–7542
- Ungár T, Dragomir I, Révész Á, Borbély A (1999) The contrast factors of dislocations in cubic crystals: the dislocation model of strain anisotropy in practice. *J Appl Crystallogr* 32:992–1002
- Ungár T, Ribárik G, Balogh L (2010) Defect-related physical-profile-based X-ray and neutron line profile analysis. *Met Mater Transact A* 41:1202–1209
- Ribárik G, Jóni B, Ungár T (2019) Global optimum of microstructure parameters in the CMWP line-profile analysis method by combining Marquardt-Levenberg and Monte-Carlo procedures. *J Mater Sci Technol* 35:1508–1514
- Gubicza J, Kassem M, Ribárik G, Ungár T (2004) The microstructure of mechanically alloyed Al-Mg determined by X-ray diffraction peak profile analysis. *Mater Sci Eng A* 372:115–122
- Fátay D, Bastarash E, Nyilas K, Dobatkin S, Gubicza J, Ungár T (2003) X-ray diffraction study on the microstructure of an Al-Mg-Sc-Zr alloy deformed by high-pressure torsion. *Z Metallkd* 94:842–847
- Yuan H, Chen Z, Buslaps T, Honkimäki V, Borbély A (2018) Combined texture and microstructure analysis of deformed crystals by high-energy X-ray diffraction. *J Appl Cryst* 51:883–894
- Klepaczko JR (1975) Thermally activated flow and strain rate history effects for some polycrystalline FCC metals. *Mater Sci Eng* 18:121–135

24. Tsuji N, Toyoda T, Minamino Y, Koizumi Y, Yamane T, Komatsu M, Kiritani M (2003) Microstructural change of ultrafine-grained aluminum during high-speed plastic deformation. *Mater Sci Eng A* 350:108–116
25. Zhang B, Shim VPW (2010) Effect of strain rate on microstructure of polycrystalline oxygen-free high conductivity copper severely deformed at liquid nitrogen temperature. *Acta Mater* 58:6810–6827
26. Williamson GK, Hall WH (1953) X-ray line broadening from filed aluminium and wolfram. *Acta Metall* 1:22–31
27. Ungár T, Gubicza J, Ribárik G, Borbély A (2001) Crystallite size distribution and dislocation structure determined by diffraction profile analysis: principles and practical application to cubic and hexagonal crystals. *J Appl Cryst* 34:298–310
28. Hinds WC (1982) *Aerosol Technology: Properties, Behavior and Measurement of Airborne Particles*. Wiley, New York
29. Krivoglaž MA (1996) *X-ray and Neutron Diffraction in Non-ideal Crystals*. Springer, Berlin, New York
30. Wilkens M (1970) Theoretical aspects of kinematical X-ray diffraction profiles from crystals containing dislocation distributions. in: J.A. Simmons, R. de Wit, R. Bullough (Eds.), *NBS Fundamental Aspects of Dislocation Theory*, Spec. Publ. 317, II, Washington, DC, USA, pp. 1195–1221
31. Ungár T, Tichy G (1999) The effect of dislocation contrast on X-ray line profiles in untextured polycrystals. *Phys Status Solidi* 147:425–434
32. Borbély A, Dragomir-Cernatescu J, Ribárik G, Ungár T (2003) Computer program ANIZC for the calculation of diffraction contrast factors of dislocations in elastically anisotropic cubic, hexagonal and trigonal crystals. *J. Appl Crystallogr* 36:160–162
33. Dieter GE (1988) *Mechanical Metallurgy*. McGraw-Hill, New York
34. Borbély A, Ungár T (2012) X-ray line profiles analysis of plastically deformed metals. *C R Physique* 13:293–306
35. Ungár T, Stoica AD, Tichy G, Wang X (2014) Orientation-dependent evolution of the dislocation density in grain populations with different crystallographic orientations relative to the tensile axis in a polycrystalline aggregate of stainless steel. *Acta Mater* 66:251–261
36. Meyers MA (1994) *Dynamic Behavior of Materials*. John Wiley & Sons, New York
37. Ungár T, Tichy G, Gubicza J, Hellmig RJ (2005) Correlation between subgrains and coherently scattering domains. *J Powder Diffr* 20:366–375
38. Fan Z, Jóni B, Ribárik G, Ódor É, Zs Fogarassy, Ungár T (2019) The Microstructure and strength of a V–5Cr–5Ti alloy processed by high pressure torsion. *Mater Sci Eng A* 758:139–146
39. Cordero ZC, Knight BE, Schuh CA (2007) Six decades of the Hall-Petch effect – a survey of grain-size strengthening studies on pure metals. *Int Mater Rev* 61:495–512
40. Taylor GI (1934) The mechanism of plastic deformation of crystals. Part I -Theoretical Proc R Soc Lond A 145:362–387
41. Gubicza J, Schiller I, Chinh NQ, Illy J, Horita Z, Langdon TG (2007) The effect of severe plastic deformation on precipitation in supersaturated Al-Zn-Mg alloys. *Mater Sci Eng A* 460–461:77–85
42. Guo WG, Gao XS (2013) On the constitutive modeling of a structural steel over a range of strain rates and temperatures. *Mater Sci Eng A* 561:468–476
43. Liu MP, Jiang TH, Wang J, Liu Q, Wu ZJ, Yu YD, Skaret PC, Roven HJ (2014) Aging behavior and mechanical properties of 6013 aluminum alloy processed by severe plastic deformation. *Trans Nonferrous Met Soc China* 24:3858–3865
44. Curtin WA, Olmsted DL, Hector LG (2006) A predictive mechanism for dynamic strain ageing in aluminium-magnesium alloys. *Nat Mater* 5:875–880
45. Guo WG (2007) Dynamic strain aging during the plastic flow of metals. *Key Eng Mater* 340–341:823–828
46. Keralavarma SM, Bower AF, Curtin WA (2014) Quantum-to-continuum prediction of ductility loss in aluminium-magnesium alloys due to dynamic strain aging. *Nat Commun* 5:4604
47. Wang JJ, Guo WG, Gao XS, Su J (2015) The third-type of strain aging and the constitutive modeling of a Q235B steel over a wide range of temperatures and strain rates. *Int J Plast* 65:85–107
48. Song Y, Garcia-Gonzalez D, Rusinek A (2020) Constitutive models for dynamic strain aging in metals: strain rate and temperature dependences on the flow stress. *Materials* 13:1794
49. Yuan KB, Guo WG, Li DW, Li PH, Zhang Y, Wang PC (2021) Influence of heat treatments on plastic flow of laser deposited Inconel 718: Testing and microstructural based constitutive modeling. *Int J Plast* 136:102865

**Publisher's Note** Springer Nature remains neutral with regard to jurisdictional claims in published maps and institutional affiliations.

Springer Nature or its licensor (e.g. a society or other partner) holds exclusive rights to this article under a publishing agreement with the author(s) or other rightsholder(s); author self-archiving of the accepted manuscript version of this article is solely governed by the terms of such publishing agreement and applicable law.